3D Bioprinted Xanthan Hydrogels with Dual Antioxidant and Chondrogenic Functions for Post-traumatic Cartilage Regeneration

Yuting Chen [1, 2, #], Le Yiguan [2, 3, #], Yang Junxu [1, 4, #], Yang Yifeng [1, 2], Feng Xianjing [1, 2], Cai Jinhong [1, 2], Shang Yifeng [1, 2], Sigit Sugiarto [5, 6], Qingjun Wei[1,4, *], Dan Kai [5, 6, *] & Li Zheng [1, 2, 7,*], Jinmin Zhao [1, 2, 4, 7]

[1] Guangxi Engineering Center in Biomedical Materials for Tissue and Organ Regeneration, The First Affiliated Hospital of Guangxi Medical University, Nanning, 530021, China.

[2] Collaborative Innovation Centre of Regenerative Medicine and Medical BioResource Development and Application Co-constructed by the Province and Ministry, The First Affiliated Hospital of Guangxi Medical University, Nanning, 530021, China.

[3] Department of Gastrointestinal Surgery, The Second Affiliated Hospital of Nanchang University, Nanchang, 330008, China.

[4] Department of Orthopaedics Trauma and Hand Surgery, The First Affiliated Hospital of Guangxi Medical University, Nanning, 530021, China.

[5] Institute of Sustainability for Chemicals, Energy, and Environment (ISCE2), Agency for Science, Technology, and Research (A*STAR), 2 Fusionopolis Way, Innovis, #08-03 Singapore 138634, Republic of Singapore

[6] Institute of Materials Research and Engineering (IMRE), Agency for Science, Technology and Research (A*STAR), 2 Fusionopolis Way, Innovis #08-03, Singapore 138634, Republic of Singapore [7] Guangxi Key Laboratory of Regenerative Medicine, The First Affiliated Hospital of Guangxi Medical University, Nanning, 530021, China.

[#] These authors contributed equally: Yuting Chen, Yiguan Le & Junxu Yang

* Corresponding author.

E-mail: weiqingjungxnn@163.com (Q. Wei), kaid@imre.a-star.edu.sg (D. Kai), zhengli224@163.com (L. Zheng)

Abstract

Intra-articular trauma typically initiates the overgeneration of reactive oxidative species (ROS), leading to post-traumatic osteoarthritis and cartilage degeneration. Xanthan gum (XG), a branched polysaccharide, has shown its potential in many biomedical fields, but some of its inherent properties, including undesirable viscosity and poor mechanical stability, limit its application in 3D printed scaffolds for cartilage regeneration. In this project, we developed 3D bioprinted XG hydrogels by modifying XG with methacrylic (MA) groups for post-traumatic cartilage therapy. Our results demonstrated that the chemical modification optimized the viscoelasticity of the bioink, improved printability, and enhanced the mechanical properties of the resulting scaffolds. The XG hydrogels also exhibit decent ROS scavenging capacities to protect stem cells from oxidative stress. Furthermore, $XGMA_{(H)}$ (5% MA substitution) exhibited superior chondrogenic potential *in vitro* and promoted cartilage regeneration *in vivo.* These dual-functional XGMA hydrogels may provide a new opportunity for cartilage tissue engineering.

Keywords

Polysaccharide; Biomaterials; Photocrosslinking; 3D Printing; ROS; Tissue Engineering

1. Introduction

Mechanical trauma, like intra-articular lesions, is one of the major risk factors for post-traumatic osteoarthritis (PTOA) with an incidence of over 50% at 20 years. In general, without proper treatment after an anterior cruciate ligament injury or another cartilage injury, there will be secondary damage to the knee cartilage and meniscus, resulting in hypersteogenesis, joint degeneration, joint space narrowing, and ultimately PTOA[1]. One of the main features of PTOA is the overexpression of reactive oxygen species (ROS) in the joint space, a class of single electron reduction products of oxygen, including superoxide anion ($\cdot O_2^-$), hydroxyl radical ($\cdot OH$), singlet oxygen ($^1O_2$), etc.[2]. Excessive ROS can induce chondrocyte mortality and upregulate the expression of inflammatory and catabolic factors, leading to the degeneration and destruction of the extracellular matrix (ECM), which further contributes to the progression of PTOA.

Once injured, articular cartilage can hardly heal and regenerate itself. In recent decades, stem cell-based therapy by transplanting multipotent mesenchymal stem cells (MSCs) into cartilage defects has been widely applied for cartilage regeneration[3, 4]. In particular, the introduction of appropriate scaffolds is important for chondrogenesis because scaffolds can provide a biomimetic microenvironment to ensure the adhesion, migration, proliferation, differentiation, and long-term survival of MSCs[5]. Recently, the precise printing of three-dimensional (3D) structured hydrogels by 3D bioprinting has attracted the most attention for the individualized treatment of cartilage defects[6]. However, the current tissue engineering strategy struggles to effectively scavenge excessive ROS before MSC implantation. This poses a risk to the health of both articular cartilage and subchondral bone and may lead to the potential development of post-traumatic osteoarthritis (PTOA), thereby compromising long-term therapeutic efficacy.

Xanthan gum (XG), which is derived from natural polysaccharides with favorable biocompatible and biodegradable properties, has recently shown great potential in tissue regeneration[7, 8]. XG has also been applied to OA therapy due to its similar properties to hyaluronic acid (HA), which is clinically used for OA therapy[9]. Superior to HA, XG is not easily degraded to ensure longer retention time *in vivo*[10]. Moreover, unlike traditional polysaccharides such as alginate and HA, etc., XG has an abundance of OH groups and pyruvate groups within its branched chain. The pyruvate groups possess an electron adsorption conjugation effect, which greatly improves the reaction efficiency of the OH group and ROS[11]. Previous studies have shown that XG had excellent antioxidant and anti-inflammatory activities, which could protect cartilage from oxidative stress-induced injury[12]. Mei et al. demonstrated that XG significantly reduced the expression of IL-1β, TNF-α, MMP-3, and MMP-13 in synovial fluid[13]. Similarly, Han et al. also demonstrated the cartilage protective capacity of XG, which significantly reversed the release of MMPs while increasing the expression of TIMP-1, leading to the increase of IL-1β induced cell proliferation[14]. XG is emerging as a promising bioink candidate for 3D printing due to its favorable rheological properties. It exhibits high viscosity at low shear forces while exhibiting shear thinning behavior at high shear forces. These properties can prevent the encapsulated cells from being stressed during 3D printing, demonstrating their good printability[15]. However, unmodified XG has unfavorable mechanical properties that are not comparable to cartilage, limiting its application as a bioink for cartilage tissue engineering[16]. Chemical modification or physical mixing with other compounds can improve the stability and mechanical strength of XG. Alginate, gelatin, silk fibroin, and their derivatives have been reported to form hybrid hydrogels with XG for 3D bioprinting[17]. Hui Pan et al. used amide-modified XG to control the mechanical strength of printable hydrogel inks[18]. Despite the improved printability, the antioxidant properties of XG may be compromised or altered, resulting in suboptimal tissue engineering repair outcomes.

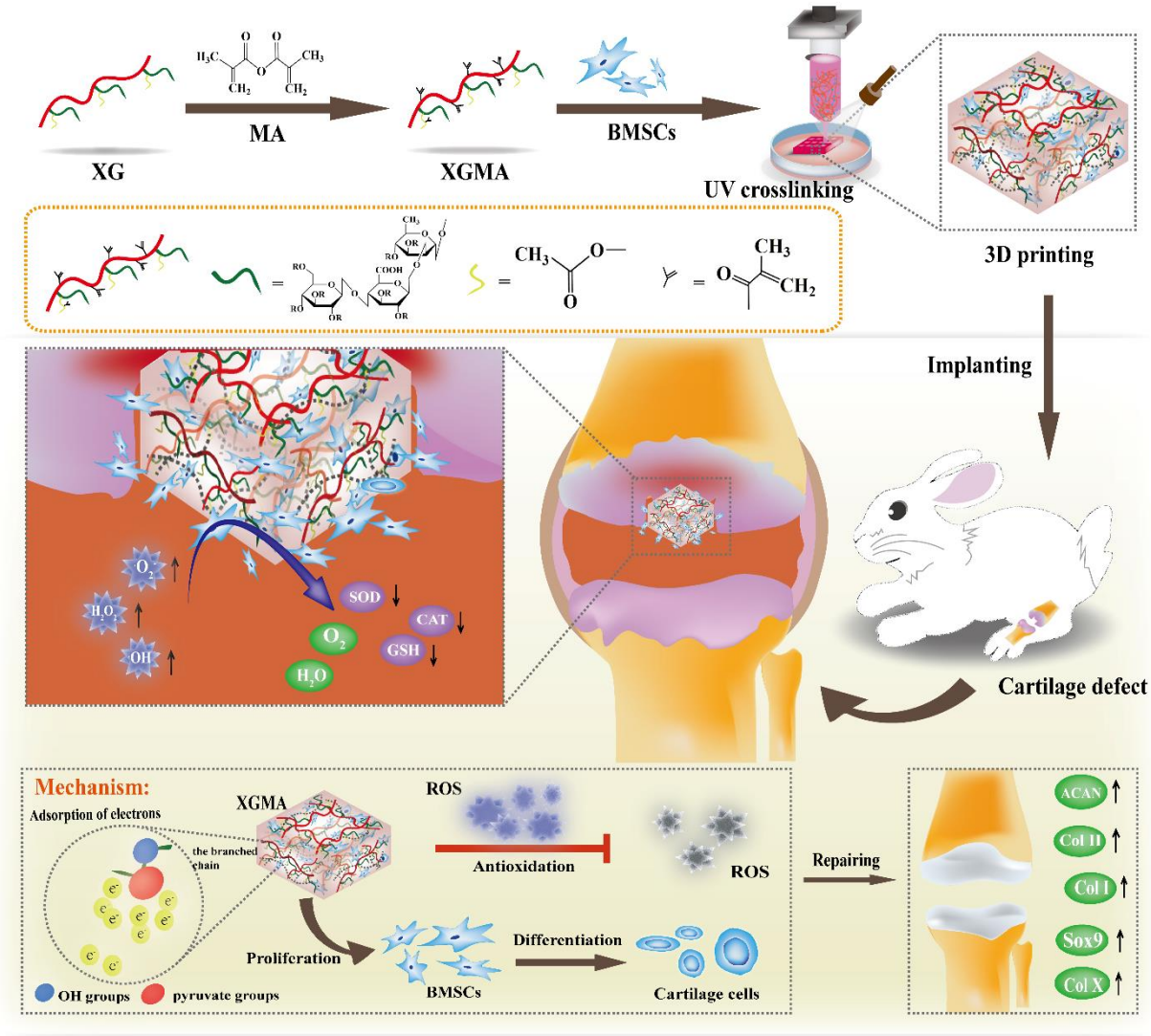

Fig. 1. Schematic illustration of the fabrication of 3D bioprinted methacrylated modified xanthan (XGMA) hydrogel scaffold and its antioxidant, anti-inflammatory, and chondrogenic directional differentiation capacity for cartilage defect repair in a rabbit model knee joint.

In this study, we hypothesize that the methacrylation of xanthan hydrogels can optimize their rheological properties and enable 3D printability. With the inherent antioxidant activity, the 3D-printed xanthan hydrogels can scavenge ROS and promote chondrogenesis for cartilage regeneration. Here, XG was modified with methacrylic (MA) groups to generate photocrosslinkable hydrogels for 3D printing. The 3D-printed scaffolds were loaded with bone marrow-derived mesenchymal stem cells (BMSCs) to form a cell-scaffold composite for PTOA therapy. The antioxidant and chondro-inductive capabilities of 3D bioprinted XGMA scaffolds

were evaluated both *in vitro* and in a trauma-induced articular cartilage lesion model (Figure 1).

2. Materials and Methods

2.1. Materials and Reagents

Xanthan gum (XG) was purchased from J&K Scientific Ltd (Shanghai, China). Collagen I (BS929, 98%) was purchased from Biosharp (Hefei, China). Sodium alginate and ferric chloride ($FeCl_3$) were purchased from Aladdin Biochemical Technology Co. Ltd (Shanghai, China). 2-Hydroxy-1-(4-(hydroxyethyl)phenyl)-2-methyl-1-propanone (Irgacure 2959), methacrylic anhydride (MAA), Hoechst 33342, chondroitin sulfate, ascorbic acid, and dexamethasone were purchased from Sigma Aldrich (St. Louis, MO, USA). TGF-β1 was purchased from PeproTech (Rocky Hill, PA, USA). Insulin-transferrin-selenium (ITS) and MEM alpha basal medium were purchased from Gibco (Grand Island, New York, USA). Fetal bovine serum (FBS) was purchased from Zhejiang Tian Hang Biotechnology Co., Ltd (Huzhou, Zhejiang, China). Proteinase K and RNA isolation kits were purchased from Tiangen Biotechnology (Beijing, China). A reverse transcription kit was purchased from Takara (Tokyo, Japan). Fast Start Universal SYBR Green Master Mix was purchased from Rochen (Germany). The live/dead kit was purchased from Invitrogen (Eugene, Oregon, USA). Pentobarbital sodium, penicillin-streptomycin, modified Safranin O- fast green FCF cartilage staining kit, hematoxylin, and eosin (HE) staining kit, trypsin-EDTA solution, micro-catalase (CAT) assay kit, micro-superoxide dismutase (SOD) assay kit, micro-glutathione peroxidase (GSH-Px) assay kit, micro-malondialdehyde (MDA) assay kit, micro-hydroxyl free radical scavenging capacity assay kit, and superoxide anion scavenging capacity assay kit, and cellulose dialysis membranes (MWCO 8~ 14 kDa) were purchased from Solarbio Science and Technology Co., Ltd (Beijing, China). Rabbit Superoxide Dismutase (SOD) ELISA Research Kit, Rabbit Catalase (CAT) ELISA Research Kit, Rabbit Glutathione Peroxidase (GSH-Px) ELISA

Research Kit, and Rabbit Malondialdehyde (MDA) ELISA Research Kit were purchased from Meimian Industrial Co., Ltd (Jiangsu, China). The primary antibodies with or without FITC label were purchased from Boster Biological Technology Co., Ltd (Wuhan, China). The general SP-9000 kit was purchased from Beijing Zhongshan Jinqiao Biological Technology Co., Ltd (Beijing, China). All chemicals were used without further purification and all kits were applied according to the protocols.

2.2. Preparation and Characterization of XGMA

Preparation of XG: Add 1 packet of PBS powder to 2000 mL of double-distilled water according to the PBS buffer preparation instructions place in a constant-temperature magnetic stirrer and stir well to dissolve the powder thoroughly. Add 150 mL of the prepared PBS buffer to a 500 mL flask and weigh 1 g of xanthan gum powder on an analytical balance. Slowly add it along the center of the flask, stirring vigorously during addition to reduce xanthan sticking to the wall and aggregating into lumps, and place it in a constant-temperature oscillator at room temperature with vigorous shaking overnight to dissolve the xanthan completely.

Modification of XG: The flask containing fully dissolved and uniformly dispersed xanthan gum solution was transferred to a collector-type magnetic stirrer equipped with dimethylsilicon oil, and the heating temperature was adjusted to 50°C. After the temperature was stabilized, 0.5 mL or 2 mL of 94% purity methylpropionic anhydride was slowly added by pipette and thoroughly stirred, and the pH of the reaction system was adjusted between 8-10 using sodium hydroxide with the concentration of 5 mmol/L. Adjust the pH between 8-10 every 30 minutes, after 6 hours of reaction, stop heating and slowly add 250mL of double-distilled water and stir to complete the reaction, cool. Dialysis bag according to the instructions of use of treatment and washing, using a pasteurized pipette to suck the end of the reaction solution into the dialysis bag (Spectra/Por®6 dialysis membrane, MWCO: 3.5 kD), the use of ultrapure water dialysis for 5-7 days, the end of dialysis began to lyophilize, lyophilized for 48 hours to obtain a white fluffy spongy modified xanthan gum methacrylate (XGMA), sealed in tin foil to protect from

light, and stored in the -20°C refrigerator. The product is sealed in aluminum foil and stored in a refrigerator at -20°C. XG and XGMA were then characterized by proton nuclear magnetic resonance spectroscopy (^{1}H NMR) with an Agilent Technologies 800/54 (USA) equipped with a temperature-adjustable system, and Fourier transform infrared spectroscopy (FTIR) recorded on a Spectrum 100 PerkinElmer FTIR.

2.3. Preparation of XGMA Ink for Screening 3D Printing Concentrations

Lyophilized XGMA was ground to powder in a clean and dry mortar, and the photoinitiator solution was prepared by dissolving Irgacure 2959 [1‰ (w/v)] in phosphate-buffered saline (PBS) at room temperature. The appropriate amount of XGMA powder was weighed and dissolved in the photoinitiator solution to prepare XGMA precursor solutions with weight percentages (Wt%) of 2%, 4%, and 6%. Each group of precursor solution into the barrel, loaded into the printer and attached to the valve connector. A 3D printer connected to the computer and air compressor equipped with printing software, the model to be printed, the machine platform height debugging and other preparations, adjust the printing air pressure in 0.050-0.060MPa, set the printing speed 5-10mm/s, select the diameter of 260 μm size of the needle, in the 3D plotter system (Regenovo, Zhejiang, China) on the Repetier software (Repetier host 1. 6.2, Germany), began to print layer by layer, the needle rises 200 μm after each layer of the print. according to the shape of the print and the printing needs of the air pump pressure to select the appropriate XGMA concentration for subsequent experiments.

2.4. Preparation of hydrogels

The XG-Fe^{3+} hydrogel was prepared as follows. Specifically, XG was dissolved in phosphate-buffered saline (PBS, pH=7.4) buffer at the weight ratio of 6%, and the post-printing XG solution was immersed in $FeCl_3$ solution (0.8%) to form physically crosslinked hydrogel (XG-Fe^{3+}). In addition, for XGMA hydrogel, lyophilized XGMA was dissolved in PBS at a weight ratio of 2%, 4%, or 6% with 0.1% (w/v) Irgacure 2959. The corresponding XGMA hydrogels were prepared by exposing the solutions to UV light (6 mV/cm^2, 365 nm, Landun

UV lamp) for 1 min at room temperature. Type I collagen hydrogel was prepared as previously described[19-21]. Briefly, 10 mg/mL collagen was dissolved in CH_3COOH solution and neutralized with 0.5 M NaOH. Then, the above solution was kept under 4℃ to avoid unwanted gelation before use. Collagen scaffolds were incubated at 37°C for 15 min to allow gelation. Specifically, the alginate hydrogel was prepared by mixing 20 mL of 6% alginate solution with 100 μL of $CaCl_2$ solution (60 mM).

2.5. Basic characterization of hydrogels

The morphology of the hydrogel scaffolds was coated with gold and characterized by scanning electron microscopy (SEM, SU-8020, Hitachi, Japan). And the swelling behavior of the hydrogels was simply tested by the gravimetric method. The hydrogels were soaked in PBS at 37 °C after lyophilization and weighed at the given time points (0, 0.5, 1, 2, 6, 12, 24, and 48 h). The swelling rate (Sr) was defined by the following equation: $Sr = (W_s - W_d) / W_s \times 100\%$, where W_d and W_s are the dry weight and swollen weights of the hydrogels, respectively. In addition, the *in vitro* degradation characteristics of the hydrogel scaffolds were also investigated by the gravimetric method. The scaffolds were immersed in the PBS buffer with shaking (60 rpm) at 37°C and weighed at the predetermined time points (0, 0.5, 1, 2, 4, 8, 16, 32, and 64 days). The degradation rate (Dr) was defined by the equation: $Dr = (W_0 - W_t) / W_0 \times 100$ (%), where W_0 was the initial dry weight of the hydrogels and W_t was the dry weight at the respective time points. The serum stability of the scaffolds was determined by immersing the hydrogel scaffolds in the cell culture medium (containing fetal bovine serum, 10% v/v) for 24 hours and then removing them for observation. Finally, the compressive modulus of the hydrogel scaffolds was determined using the Compressive Strength Tester HY-0230 (Shanghai, China). Briefly, the scaffolds were placed on the base and compressed at a rate of 0.5 mm/min. The pressure sensor continuously recorded the compressive strength data until the hydrogel scaffolds were destroyed.

2.6. Rheological study of hydrogels

The rheology of hydrogel scaffolds was investigated using ARES-G2 (TA Instruments, USA) with a 20 mm palette. The hydrogels, with a radius of 10 mm and a height of 1 mm, were evaluated with dynamic frequency, oscillatory strain, and temperature sweeps, and the edge of the scaffolds was covered with ultra-low viscosity silicone fluid (viscosity of 5 CST at 25°C, Clearco, USA) to avoid sample drying. For pre-gel solutions, 200 μL samples were tested with a measuring gap of 0.5 mm. All samples were tested under linear viscoelastic conditions to measure the oscillatory rheology. Dynamic frequency scanning was performed at a fixed oscillatory strain of 1% and dynamic strain scanning was tested at a fixed angular frequency of 6.3 rad/s to measure the storage modulus (G') and loss modulus (G") at shear rates ranging from 0.1 to 100 s^{-1}at 25 °C. The oscillatory temperature ramp evaluation was performed under conditions between 20 and 40°C at a frequency of 1 Hz and an angular frequency of 6.3 rad/s.

2.7. Evaluation of ROS clearance capacity

The ROS scavenging ability of the hydrogels was evaluated using a hydroxyl radical (·OH), superoxide anion ($\cdot O_2^-$), and hydrogen peroxide (H_2O_2) scavenging capacity assay kit (Solarbio, China). Measurements were performed according to the manufacturer's instructions. For the ·OH assay, hydrogels were soaked in 750 μL PBS buffer for 6 hours, followed by the addition of 150 μL H_2O_2 for reaction, followed by the addition of 750 μL reagent mixture from the kit. The final mixture was then incubated at 37°C for an additional 1 hour and measured by UV-Vis spectroscopy at 536 nm. Similarly, for the $\cdot O_2^-$ scavenging capacity assay, hydrogels were first immersed in 100 μL PBS buffer for 6 hours, followed by the addition of 300 μL reagents according to the manufacturer's instructions. After incubation, the fluids were measured by UV-Vis spectroscopy at 536 nm. For the H_2O_2 assay, the hydrogels were immersed in 750 μL of PBS buffer, followed by the addition of 1 mL of H_2O_2 (1 mM). The mixture was incubated at 37°C for 1 hour and measured by UV-Vis spectroscopy at 411 nm before mixing it with 25 μL of the appropriate reagents.

2.8. Cell isolation and culture

Bone marrow mesenchymal stem cells were obtained from 3-day-old New Zealand rabbits provided by Guangxi Medical University and approved by the ethics committee for in vitro study. Newborn New Zealand White rabbits were killed, the femur and humerus were removed, and the muscles and ligaments were excised. The bone marrow cavity was washed with α-MEM medium (containing 10% fetal bovine serum and 1% penicillin/streptomycin) and incubated at 37°C in a 5% CO_2 atmosphere. When adherence reached 90%, the cells were digested with trypsin for passage culture.

2.9. 3D bioprinting of hydrogel scaffolds

BMSCs were encapsulated in XG, XGMA, collagen, or alginate solutions at 1×107 cells/mL density to form bioinks before 3D bioprinting. The prepared bio-inks were printed using an extrusion-based 3D bioprinter (Regenovo, Zhejiang, China) with a 260 μm diameter nozzle and 0.050~0.060 MPa air pressure. The bio-inks were then deposited layer by layer with the 3D bioprinter at a constant extrusion speed of 5~ 10 mm/s, forming the designed scaffolds. XG and XGMA scaffolds were both printed at room temperature. XGMA scaffold was prepared by exposing the scaffold to UV light (6 mV/cm^2, 365 nm, Landun UV lamp). XG scaffold was cross-linked using $FeCl_3$ solution (0.8%) to form a physically crosslinked hydrogel 3D printed scaffold (XG-Fe^{3+}). The collagen bioink was filled into the cap of a 4 mL Eppendorf tube and then placed at 37°C to promote collagen bioink gelation. Alginate bio-ink was gelated by mixing 20 mL of 6% alginate solution, cell loaded, with 100 μL of $CaCl_2$ solution (60 mM), and the mixed solution was used for bioprinting. The entire bio-printing process was controlled within 2 minutes to ensure cell viability and the 3D printer was sterilized using ultraviolet before use. The printed 3D scaffolds were cultured with cell culture medium at 37°C in a 5% CO_2 atmosphere for 20 min to remove unreacted components, then the culture medium was renewed.

2.10. The stress-strain curve of cured XGMA was measured on an Instron 5943 universal materials testing machine (Instron Engineering Corporation, Norwood, MA, USA) at a travel speed of 0.5 mm/min. Specimens were prepared in a mold (5 mm diameter and 5 mm height). The fatigue resistance of XGMA was tested on an Instron E1000 fatigue tester (Instron Engineering Corporation, Norwood, MA, USA). The compressive modulus was calculated from the slope of the linear region (10% ~ 20% strain) on the stress-strain curve. We also compared the measured Young's modulus to the normal chondrogenic environment.

2.11.Cell cytotoxicity, proliferation, and chondrocyte differentiation

The hydrogel scaffolds were cultured in a chondrogenic medium containing 10 ng/mL TGF-β for 3 or 7 days. The cytotoxicity of the hydrogel scaffolds was evaluated by live/ dead cell ratio. The samples were first stained with PBS buffer containing 2 μM calcein-AM and 4.5 μM propidium iodide for 20 minutes at room temperature and then washed three times with PBS buffer. The final samples were observed by laser scanning confocal microscopy (LSCM, Nikon A1, Japan), and the corresponding live/ dead ratio was quantified using Image J software. In addition, the hydrogel scaffolds were incubated in a chondrogenic medium containing 10 ng/mL TGF-β for 7 or 14 days. The DNA and glycosaminoglycan (GAG) content of different scaffolds were determined using the DNA Quantitation Kit (Sigma-Aldrich) and rabbit GAG ELISA Kit (Shanghai Yanqi Biotechnology Co.), respectively, according to the manufacturer's instructions. To control for variables, all scaffolds were checked at the same initial volume before culture. Expression of chondrogenic genes such as SRY-related high mobility group box gene 9 (Sox 9), aggrecan (ACAN), collagen II (Col II), and fibrotic marker genes such as collagen type X (Col X) and collagen type I (Col I), were analyzed by quantitative reverse transcriptase polymerase chain reaction (qRT-PCR) using the LightCycler® 96 system (Roche, Switzerland). The detailed primer sequences are listed in Table S3, and the $2^{-\Delta\Delta Ct}$ method was used to assess gene expression levels, with glyceraldehyde-3-phosphate dehydrogenase

(GAPDH) as an internal reference. At both time points, the alginate group was used as the negative control group and its gene expression level as the normalization factor.

2.12. Cell adhesive ability

The hydrogel scaffolds were placed on the cell-climbing sheet and sterilized after UV exposure. Then, BMSCs at a density of 5.0×10^4 cells/mL were seeded on the surface of the hydrogel scaffolds and cultured with a growth medium. The cultured BMSCs were observed by laser scanning confocal microscopy (LSCM, Nikon A1, Japan) after staining F-actins with FITC-phalloidin (green) and nuclei with 2-(4-aminophenyl)-6-indolecarbamidine dihydrochloride (DAPI, blue).

2.13. Antioxidant ability of hydrogel scaffolds

The scaffolds were seeded with MSCs (1×10^7 cells/mL) and cultured in a chondrogenic medium containing 400 μM H_2O_2 for 24 h. The viability of H_2O_2-induced BMSCs was also examined by live/ dead cell ratio as described above. The samples were immersed in the staining solution for 20 minutes and imaged by laser scanning confocal microscopy. Meanwhile, the expression of antioxidant genes such as CAT, SOD, and GSH-Px was analyzed by quantitative reverse transcriptase polymeric chain reaction (qRT-PCR) after total RNA was collected from BMSCs. In addition, the expression of proteins: CAT, SOD, GSH-Px, and MDA were quantitatively determined by enzyme-linked immunosorbent assay (ELISA) according to the manufacturer's instructions.

In addition, the ability of the hydrogels to scavenge ROS and $\cdot O_2^-$ was detected using the fluorescent probe DCFH-DA (Beyotime, China) and the fluorescent probe DHE (Beyotime, China), respectively. MSCs were used for the intracellular ROS scavenging assay. The positive control reagent for ROS was H_2O_2 at a final concentration of 400 μM. Cells (1.5×10^4) were cultured in 12-well plates for 24 h and then incubated with PBS, H_2O_2 and alginate hydrogel, H_2O_2 and collagen hydrogel, H_2O_2 and XG-Fe^{3+}, H_2O_2 and XGMA for 24 h. A blank group (no

hydrogel and H_2O_2) was also established. The probe (10 μM) was co-incubated with the cells for 30 min and then analyzed by fluorescence microscopy (BD Biosciences, USA).

2.14. In vivo animal investigation

Thirty New Zealand White rabbits (3~3.5 kg, 3~4 months) were approved by the Experimental Animal Center of Guangxi Medical University. All the experiments were conducted according to the guidelines of the Animal Research Ethics Committee of the Guangxi Medical University (Protocol Number: 201606190). By the standards for animal housing, New Zealand White rabbits were group-housed in an atmosphere of 23 ℃ to 25 ℃ and allowed free access to water and standard laboratory pellets.

The cartilage defect model was constructed as follows: the rabbit was anesthetized with 1% sodium pentobarbital intravenously via the ear margin. After successful anesthesia, the rabbit's knee joint was sterilized with tincture of iodine and ethanol, and a sterile drape was applied. Avoiding subcutaneous blood vessels, the skin, subcutaneous tissue, and fascia were incised obliquely with a 2.0-cm incision, exposing the lateral epicondyle of the femur, dissecting the attached tendon, and exposing the femoral stem and femoral condylar diaphysis. A regular cylindrical defect of 4 mm in diameter and 2 mm in depth was drilled at the center of the femoral trochlear of the hind leg, and then a hydrogel scaffold was implanted into the defect, followed by suturing of the skin and injection of penicillin to prevent infection.

The rabbit models were randomized into the following groups: (1) untreated (control), (2) alginate, (3) collagen, (4) XG-Fe^{3+}, and (5) $XGMA_{(H)}$. After 12 weeks, the rabbits were anesthetized and killed with an overdose of pentobarbital, and the repaired articular cartilage was harvested. Macroscopic evaluation of the cartilage was performed according to the International Cartilage Repair Society (ICRS) scoring criteria as described in the literature[22, 23]. In addition, the articular cartilage was fixed with 4% (v/v) paraformaldehyde for 48 hours, followed by decalcification with ethylenediaminetetraacetic acid (EDTA, pH 7.2) for 4 weeks. Dehydration was achieved with a gradient concentration of ethanol before paraffin embedding

and cutting into 8 μm thick sections. The tissue slides were examined by hematoxylin & and eosin (HE), safranin O/ fast green, and immunohistochemical (Col II) staining. Finally, the slides were examined by light microscopy (BX53, Olympus, Japan) and graded according to the histologic/histochemical grading system (HHGS).

2.15. Statistical analysis

The data was expressed as mean ± standard deviation (SD). The quantification data of cell cytotoxicity and proliferation assay in *2.11* and the experiment data in section *2.13* (excepting the quantification of fluorescent probe test) were analyzed using two-way analysis of variance (ANOVA) and the Bonferroni test is used for correcting test statistics. In other experiments, the statistical difference between various groups was evaluated using one-way ANOVA or Student's t-test. (*#p< 0.05, **##p< 0.01, ***###p< 0.001, and ****####p< 0.0001).

3. Results and Discussion

3.1. Preparation and characterization of XGMA

To form a stable hydrogel for 3D printing, XG was modified with MA groups followed by UV crosslinking. As shown in Figure 2A, the hydroxyl groups of XG reacted with methacrylic anhydride (MAA) to form XGMA. Detailed reaction conditions are given in Table S1. After reaction with two different amounts of MAA, XGMA with two different degrees of substitution (DS) were prepared and defined as $XGMA_{(L)}$ and $XGMA_{(H)}$, respectively.

As shown in Figure 2B, the obvious characteristic peak at 1720 cm^{-1} corresponding to the -C=O stretching vibration of the $-COOCH_3$ group was observed for XG and XGMA. The other characteristic peaks (3425 cm^{-1} and 1627 cm^{-1}), corresponding to -OH and -C=O vibration peaks, were also found in both XG and XGMA. The results indicated that there was little change in the characteristic peaks in XGMA compared to XG. The chemical modification was also confirmed by ^1H NMR. As shown in Figure 2C, the apparent chemical shifts at 5.6 ppm and

6.2 ppm corresponding to the protons of -CH=CH_2 were observed in XGMA instead of XG. In addition, the chemical shift around 1.8 ppm (-CH_3) appeared for XGMA, which was contributed by the -OCH_3 group of XG itself and the -CH_3 group of MA of XGMA. Moreover, the chemical shift around 4.5~ 4.8 ppm in $XGMA_{(H)}$ was stronger than that in $XGMA_{(L)}$, indicating more protons for $XGMA_{(H)}$ with higher DS. Finally, the DS of MA groups was evaluated by comparing the chemical shifts of -CH=CH_2 (Figure 2C(a)) and -OCH_3 (Figure 2C(b)). According to the calculation, the DS of MA was 1.4% for $XGMA_{(L)}$ and 5% for $XGMA_{(H)}$ (Table S1).

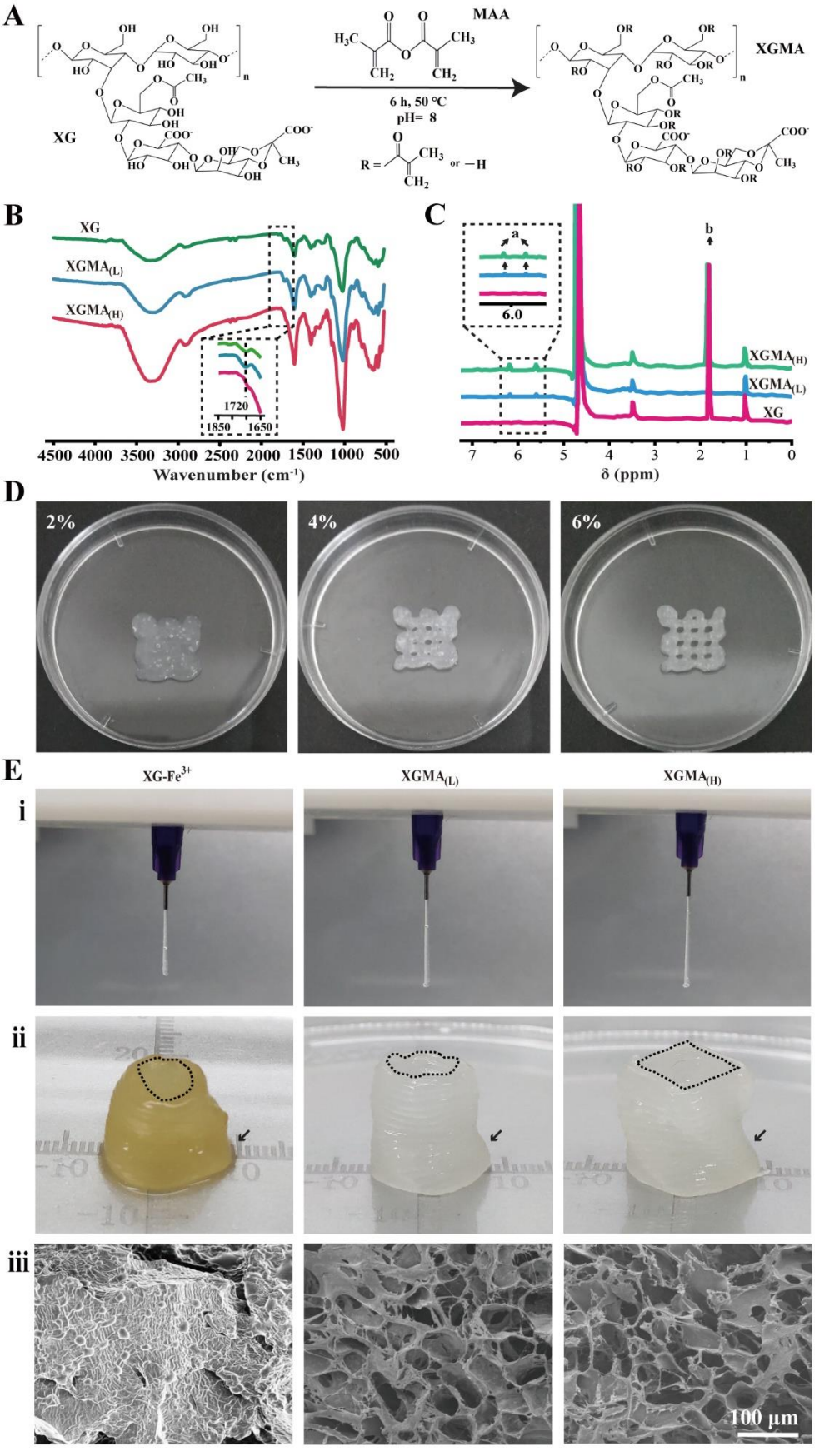
A
XG
MAA
6 h, 50 °C
pH= 8
R = CH3 or −H
XGMA
B
XG
XGMA(L)
XGMA(H)
1720
1850 1650
4500 4000 3500 3000 2500 2000 1500 1000 500
Wavenumber (cm-1)
C
a
b
6.0
XGMA(H)
XGMA(L)
XG
7 6 5 4 3 2 1 0
δ (ppm)
D
2%
4%
6%
E
XG-Fe3+
XGMA(L)
XGMA(H)
i
ii
iii
100 μm

Fig. 2. A) Synthetic pathway of XGMA by the chemical reaction between XG and methacrylic anhydride (MAA). B) FTIR and C) ^{1}H NMR results of XG, $XGMA_{(L)}$, and $XGMA_{(H)}$. D) Macroscopic images of 3D printed $XGMA_{(H)}$ scaffolds at 2%, 4%, and 6% weight concentration. E) 3D printability of XG-Fe^{3+}, $XGMA_{(L)}$, and $XGMA_{(H)}$ and their corresponding SEM images.

3.2. 3D printability of hydrogels

To determine the optimal print concentration of XGMA hydrogel, its shape fidelity is examined in this section. First, the rheological properties of pre-gel solutions with different concentrations of 2%, 4%, and 6% were investigated to determine a suitable bioink formulation. As shown in Figure S1, A, the viscosity of $XGMA_{(H)}$ prequel solutions decreased from about 56.88 Pa.s to less than 3.89 Pa.s with the increase of shear rate from 0.1 1/s to 100 1/s, showing an obvious shear thinning property with the decrease of viscosity during 3D printing extrusion. Moreover, the 6% $XGMA_{(H)}$ prequel solution showed a higher viscosity than the 2% and 4% solutions in the range of shear rate except for the low shear rate (0.1 1/s) (Figure S1(B)). The apparent shear thinning was observed for XG and XGMA pre-gel solutions at a concentration of 6%. Similarly, shear thinning was also observed for $XGMA_{(H)}$ with different concentrations (2%, 4%, and 6%). In general, $XGMA_{(H)}$ pre-gel solution had higher viscosity compared to $XGMA_{(L)}$ and XG pre-gel solutions at the same concentration, which was caused by the high DS of MA groups for $XGMA_{(H)}$. The viscosity of $XGMA_{(H)}$ pre-gel solution showed the apparent concentration dependence, which increased as the concentration of the gel solution increased. This indicated that the formation of a stronger interaction influenced by the hydrogen bond and/or MA groups contributed to the improved viscosity of the materials. Furthermore, XG and XGMA pre-gel solutions maintained relatively stable viscosity as the temperature increased from 20 to 40 °C (Figure S1(C and D)), indicating that XG and XGMA pre-gel solutions could be adapted to 3D printing within a certain temperature range. In summary, XG and XGMA were confirmed as promising inks for 3D printing.

During 3D printing, the hydrogel scaffolds were printed with 8~10 layers and then crosslinked by UV irradiation for 10 min (Video S1). Figure 2D shows the $XGMA_{(H)}$ scaffolds

after UV crosslinking. It was observed that 2% $XGMA_{(H)}$ scaffold collapsed easily and 4% $XGMA_{(H)}$ scaffold showed slight collapse. However, the structure of 6% $XGMA_{(H)}$ was well preserved and no collapse was observed. This is consistent with the findings of Li and Ouyang's work[24, 25], who studied the printability of hydrogels with different concentrations to have undergelation, proper-gelation, or overgelation states. They found that only hydrogels in the proper gelation state showed suitable printability. Therefore, it is important to find the optimal printing concentration of hydrogel bioinks. In terms of morphological fidelity, we believe that a concentration of 6% is the optimized printing concentration for XGMA. In addition, the morphology of 6% $XGMA_{(H)}$ was also examined by SEM. As shown in Figure 2E, the obvious interconnected network structure was observed for $XGMA_{(H)}$, which might be beneficial for the transfer of water and nutrients for cell growth. Therefore, 6% XG and XGMA were selected for further investigation. Compared to other hydrogels (alginate, collagen, and XG-Fe^{3+}), the $XGMA_{(H)}$ shows superior printability (Figure S3), which can be printed into multilayers or different shapes (Figure S4 and Figure S5), suggesting that $XGMA_{(H)}$ possesses a wide range of three-dimensional printing behaviors.

To further evaluate the interference factor of 3D printing, three types of XG-based hydrogels were prepared: XG-Fe^{3+}, $XGMA_{(L)}$, and $XGMA_{(H)}$ were prepared followed by UV exposure. As shown in Figure 2E, all the pre-gel solutions could maintain a stable translucent filament under the pressure of 0.060 MPa and then could be printed smoothly as designed shapes. Among all the samples, $XGMA_{(H)}$ maintained its original shape better than that of $XGMA_{(L)}$, which slightly collapsed and finally formed a round corner. Furthermore, the ionic cross-linked XG-Fe^{3+} collapsed and only the approximate shape could be maintained, demonstrating that the UV cross-linked XGMA was more suitable for 3D printing than that of the ionic cross-linked XG-Fe^{3+} (Figure 2E(ii)). Meanwhile, the morphology of the XG-type hydrogels was also evaluated by SEM. As shown in Figure 2E(iii) and Figure S2, $XGMA_{(H)}$ and $XGMA_{(L)}$ exhibited the obvious interconnected 3D network structures, while XG-Fe^{3+} only

showed the disorganized aggregated structure without obvious porosity. The presence of an interconnected network was essential for cell migration and transport of small molecules such as oxygen, nutrients, metabolites, etc.[26, 27]. Thus, 6% $XGMA_{(H)}$ with favorable 3D printability and porous network structure was a perfect bio-ink for bioprinting. Overall, 3D-printed hydrogel scaffolds can not only be printed in layers but can also be prepared with anisotropic properties, allowing different regions on a scaffold to have different biological functions.

3.3. Characterization of hydrogel scaffolds

As shown in Figure 3A, XG-Fe^{3+} almost reached the swelling equilibrium after 48 h with a swelling rate of about 3570%. However, $XGMA_{(L)}$ and $XGMA_{(H)}$ reached equilibrium within 24 h, and their corresponding equilibrium swelling ratios decreased by 20.1% for $XGMA_{(L)}$ and 64.0% for $XGMA_{(H)}$, respectively. The degradation rate of the hydrogels is shown in Figure 3B. It was observed that the degradation rate of XG-Fe^{3+} was close to 90%, while it was only 76% for $XGMA_{(L)}$ and 48% for $XGMA_{(H)}$ after 60 days. The above results indicated that chemical crosslinking by MA groups, especially at high DS levels, had a greater effect on the water retention and degradation rate of XG hydrogels than ionic crosslinking.

Structural stability in culture medium is important for 3D-printed scaffolds for further cell culture[28-30]. As shown in Figure 3C, it was observed that XG was almost completely dissolved in the medium, while XG-Fe^{3+} and XGMA almost maintained their shape after 24 h of immersion. In particular, $XGMA_{(H)}$ kept its original shape intact. To further investigate the mechanical properties, the compressive modulus of the scaffolds was also evaluated by immersing the scaffolds in the culture medium for 24 h. As shown in Figure 3D, the compressive modulus for XG-Fe^{3+} was around 393 kPa at the beginning, while it decreased extremely by 99.6% after immersing in the culture medium for 24 h. The remarkable decrease in the compressive modulus after immersion was due to the weak bond of ionic crosslinking in XG-Fe^{3+}, which could be easily affected by the diffusion of ions in the medium. Conversely,

the reduction in compressive modulus of $XGMA_{(L)}$ and $XGMA_{(H)}$ after a 24-hour immersion was only 20.7% and 18.9%, respectively, with only slight swelling. The results proved that chemically cross-linked XGMA could better maintain structural stability in the medium than ionic cross-linked XG-Fe^{3+}.

As shown in Figure S6, the compressive stress of XGMA is 9.0 KPa in the 10% to 20% strain range, which is close to the mechanical environment of cartilage formation (10 KPa)[31, 32].

The rheological behavior of the hydrogels was evaluated by three modes: angular frequency variation, oscillatory strain, and temperature sweep. In general, the elastic properties of the hydrogels were dominant, characterized by a storage modulus (G') higher than the loss modulus (G"). As shown in Figure 3E(i), G' and G" of $XGMA_{(H)}$ with different concentrations remained relatively stable with increasing angular frequency from 0.1 to 100 rad/s, except for a slight increase at high angular frequency. Throughout the angular frequency range, G' was always higher than G" for different concentrations of $XGMA_{(H)}$, and both G' and G" for 6% $XGMA_{(H)}$ were higher than those for 2% and 4% $XGMA_{(H)}$. Similarly, G' and G" of $XGMA_{(H)}$ with different concentrations maintained almost the same modulus from 20 to 40°C (Figure 3E(ii)). In particular, G' gradually decreased and G" slowly increased for $XGMA_{(H)}$ by increasing the oscillatory strain from 0.1% to 100%. It was also possible to observe the appearance of the gel point for 2%, 4%, and 6% $XGMA_{(H)}$ above 100% oscillatory strain (Figure 3E(iii)). Meanwhile, the rheological behavior of different types of hydrogels was also investigated. G' and G" of XG-Fe^{3+}, $XGMA_{(L)}$, and $XGMA_{(H)}$ with the same concentration of 6% remained stable in both angular frequency and temperature sweep modes (Figure 3E (iv and v)). Specifically, the order of G' and G" was: $XGMA_{(H)}$> XG-Fe^{3+}> $XGMA_{(L)}$. And the G' of all the hydrogels decreased and their G" increased with the increase of the oscillatory strain.

It was also possible to obtain the gel point for all hydrogels when the oscillatory strain was above 100% (Figure 3E(vi)). In general, $XGMA_{(H)}$ showed stable rheological behavior at different concentrations, especially for 6% $XGMA_{(H)}$ with the highest G' (up to 3575 kPa),

which is close to the stiffness of cartilage. Among the three different types of hydrogels, $XGMA_{(H)}$ presented the highest G' and G" due to the highest degree of chemical cross-linking. Nevertheless, XG-Fe^{3+} exhibited better rheological behavior than that of $XGMA_{(L)}$, indicating that the low degree of chemical crosslinking could not sufficiently support the hydrogel network structure.

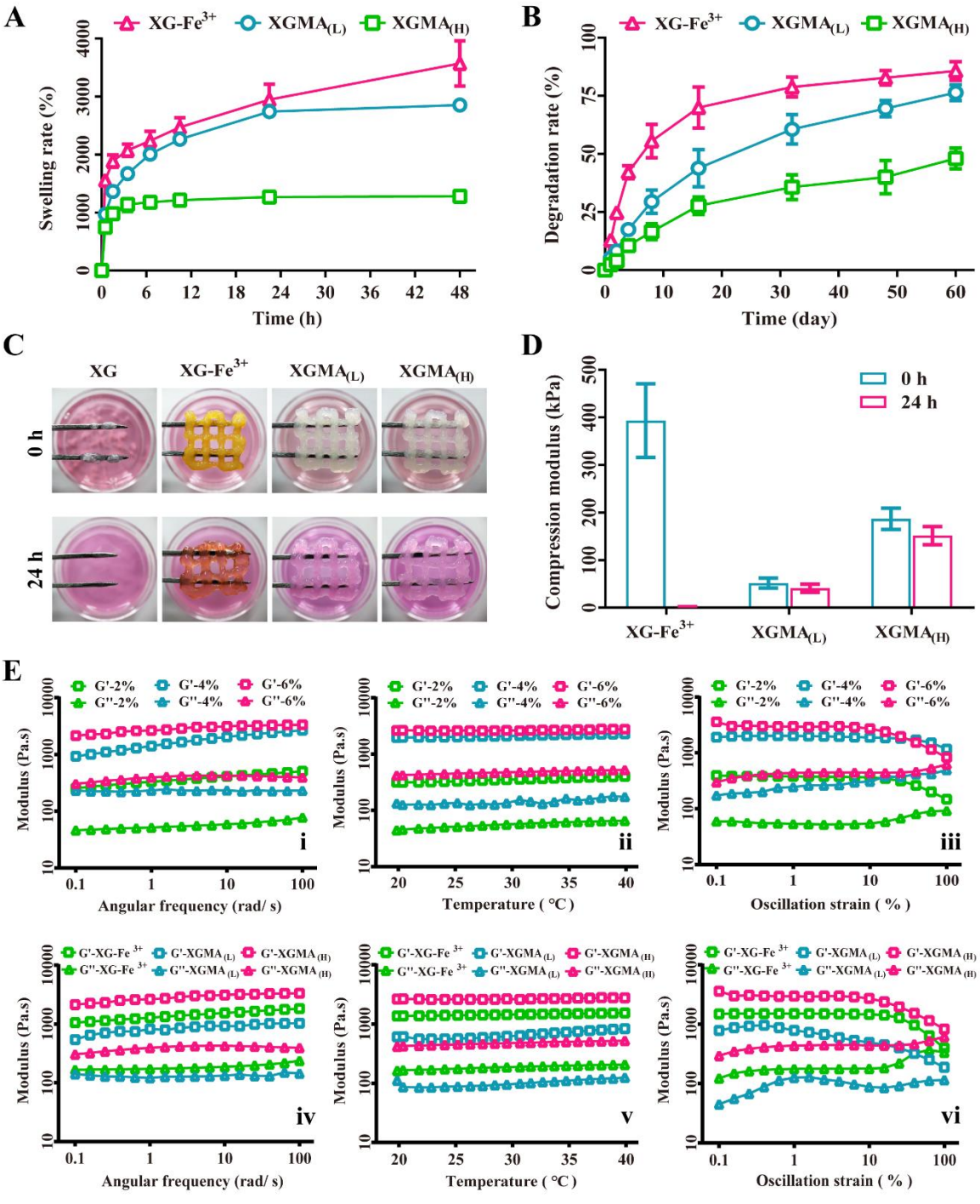

Fig. 3. Physical characterization of the hydrogel scaffolds. A) Swelling rate of XG-Fe^{3+}, $XGMA_{(L)}$, and $XGMA_{(H)}$. B) Degradation rate of XG-Fe^{3+}, $XGMA_{(L)}$, and $XGMA_{(H)}$. C) Stability of XG, XG-Fe^{3+}, and $XGMA_{(H)}$ in culture medium and their corresponding compressive modulus before and after immersion in culture medium for 24 h (D). E) Rheological behavior (storage modulus (G') and loss modulus (G")) of hydrogels: (i) $XGMA_{(H)}$ with the concentration of 2%, 4% and 6% in angular frequency, (ii) oscillatory strain and (iii) temperature sweep modes, and 6% XG-Fe^{3+}, $XGMA_{(L)}$ and $XGMA_{(H)}$ in (iv) angular frequency, (v) oscillatory strain and (vi) temperature sweep modes.

3.4. ROS scavenging capacity

The excessive ROS played a negative role during the cartilage regeneration process, leading to articular cartilage damage and further inducing PTOA. It was expected that hydrogel scaffolds would have a favorable ROS scavenging ability, which would help improve cartilage repair. Alginate, known for its favorable properties in cell attachment and growth, has been widely used in 3D bioprinting, accompanied by Ca^{2+} crosslinking[33-35]. Although collagen is not suitable for printing, its chondrogenic potential has been widely applied in cartilage tissue engineering[36]. Therefore, 3D-printed alginate and non-printed collagen were used as a reference for further investigation, in comparison with XGMA. The ROS scavenging capacity of the hydrogels was evaluated using the ·OH, $\cdot O_2^-$, and H_2O_2 scavenging capacity assay kits, respectively. As shown in Figure S7, $XGMA_{(H)}$ exhibited an ·OH scavenging rate of 11.97%, which was higher than that of XG-Fe^{3+}, collagen, and alginate, which showed a 1.15-fold, 3.24-fold, and 4.49-fold increase, respectively. This trend was consistent with the scavenging rate for both $\cdot O_2^-$ and H_2O_2. Thus, XGMA(H) had the optimal ROS scavenging capacity, followed by XG-Fe^{3+}, collagen, and alginate. Although some of the OH groups were modified, a large amount of OH groups were still present in $XGMA_{(H)}$. In addition, the presence of the unique pyruvate group of XG was helpful for the strong adsorption of ROS, which further contributed to the enhanced ROS scavenging capacity.

3.5. Cell cytotoxicity of hydrogels

The cytotoxicity of the hydrogel scaffolds was evaluated by the live/ dead ratio. The hydrogel scaffolds were prepared after loading with BMSCs, followed by incubation in a culture medium for 3 and 7 days. As shown in Figure 4A, only a few live cells were observed in 3D-printed alginate, while a significant population of live cells was evident in collagen at day 3. Remarkably, many live cells appeared in $XGMA_{(H)}$, while some live cells were found for 3D-printed XG-Fe^{3+} on day 3. By day 7, cells proliferated slightly in all scaffolds. However, the consistent trend of the number of live cells remains alginate < XG-Fe^{3+} < collagen < $XGMA_{(H)}$ on day 7. After statistical analysis, the live/ dead ratio was 49.6% for alginate, which increased to 92.2%, 79.9%, and 99.6% for collagen, XG-Fe^{3+}, and $XGMA_{(H)}$, respectively, on day 3. At day 7, almost equivalent live/ dead ratios were observed for alginate (62.3%) and XG-Fe^{3+} (66.2%). However, the live/ dead rates of collagen and $XGMA_{(H)}$ were 89.4% and 98.6%, respectively (Figure 4B). Among these scaffolds, $XGMA_{(H)}$ exhibited the highest cell viability, demonstrating its favorable biocompatibility, as shown in Figure S8. The study also showed that UV exposure and the presence of 0.1% initiator in the $XGMA_{(H)}$ had minimal cytotoxicity on the cells, consistent with the previously reported results[37]. In contrast, XG-Fe^{3+} showed obvious cytotoxicity, which could be attributed to the introduction of Fe^{3+}.

3.6. BMSCs proliferation and chondrogenic activity

Cell DNA content was used to evaluate the proliferation of BMSCs within hydrogel scaffolds cultured in a chondrogenic medium for 7 and 14 days. As shown in Figure 4C(i), the DNA content at day 7 was in the order of alginate < XG-Fe^{3+} < collagen < $XGMA_{(H)}$, corresponding to cell cytotoxicity. At day 7, the DNA content for all scaffolds still maintained the same trend with a slight increase. Meanwhile, GAG was used to assess the secretion of aggrecan, which is a specific chondrogenic biomarker. Among the scaffolds, the GAG/DNA ratio of $XGMA_{(H)}$ was highest on day 3 and day 7, which was even significantly higher than collagen on day 7. While XG-Fe^{3+} and alginate showed the lowest expression of GAG content

for chondrogenesis. As a result, the GAG content increased with time for all groups (Figure 4C(ii)). Based on the above results, $XGMA_{(H)}$ exhibited the optimal potential for BMSC differentiation into chondrocytes, followed by collagen.

In addition, the gene expression of BMSCs in each hydrogel scaffold was analyzed by qRT-PCR. At both time points (day 7 and day 14), the alginate group was used as the negative control group and its gene expression level as the normalization factor. As shown in Figure 4D, the gene expression of chondrogenic markers (Col II, ACAN, and Sox9) increased with time for all scaffolds, consistent with DNA content and GAG/DNA ratio. At the same time point, $XGMA_{(H)}$ showed the highest expression of chondrogenic markers, significantly higher than XG-Fe^{3+} and alginate. Furthermore, fibrocartilage marker Col I and hypertrophic cartilage marker Col X showed almost the opposite trend in all groups compared to the expression of cartilage-specific markers. From the above results, it was concluded that $XGMA_{(H)}$ exhibited more chondrogenic potential toward hyaline-like cartilage than XG-Fe^{3+} and alginate. Notably, this result was even better than that of collagen, as evidenced by its ability to induce chondrogenic differentiation[38].

3.7. Cell adhesion ability

The cell adhesion ability was implemented by culturing BMSCs on the surface of hydrogel scaffolds for 1 and 4 days. As shown in Figure 4E, on day 1, the stretched parapodium and actin filaments in the cytoskeleton were detected for BMSCs cultured on the surface of $XGMA_{(H)}$ compared to other scaffolds, demonstrating that $XGMA_{(H)}$ promoted the spreading of BMSCs. On day 4, $XGMA_{(H)}$ showed the best cell adhesion ability, while the worst adhesion ability occurred on XG-Fe^{3+} on day 4. Therefore, $XGMA_{(H)}$ was helpful for the attachment of BMSCs to its surface. However, a certain amount of Fe^{3+} interfered with the attachment of BMSCs on the surface of XG-Fe^{3+}, resulting in the poor adhesion of BMSCs.

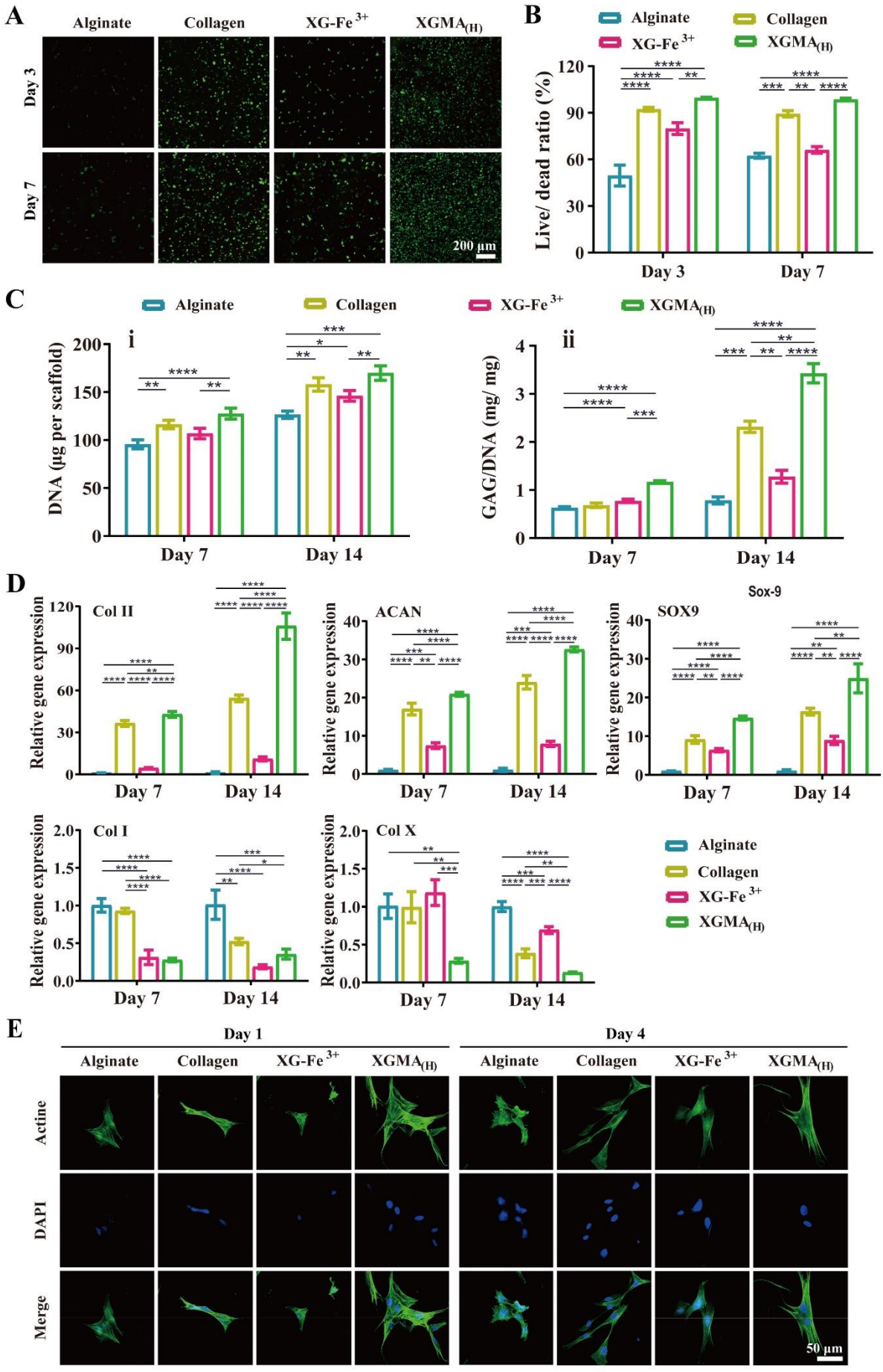
A
Alginate
Collagen
XG-Fe 3+
XGMA(H)
Day 3
Day 7
200 μm
B
Alginate
Collagen
XG-Fe 3+
XGMA(H)
Live/ dead ratio (%)
Day 3
Day 7
C
Alginate
Collagen
XG-Fe 3+
XGMA(H)
i
DNA (μg per scaffold)
Day 7
Day 14
ii
GAG/DNA (mg/ mg)
Day 7
Day 14
D
Col II
ACAN
SOX9
Sox-9
Col I
Col X
Relative gene expression
Day 7
Day 14
Alginate
Collagen
XG-Fe 3+
XGMA(H)
E
Day 1
Day 4
Alginate
Collagen
XG-Fe 3+
XGMA(H)
Actine
DAPI
Merge
50 μm

Fig. 4. A) Live/ dead staining images of BMSCs encapsulated in alginate, collagen, XG-Fe^{3+} or $XGMA_{(H)}$ after 3D bioprinting at day 3 and day 7 by confocal microscopy and B) corresponding quantified results (n= 3, *p< 0.05, **p< 0.01 and ***p< 0.001) C) DNA content and GAG/DNA ratio of BMSCs encapsulated in hydrogel scaffolds by 3D bioprinting after 7 and 14 days of induction. (n= 3, *p< 0.05, **p< 0.01, ***p< 0.001 and ****p< 0.0001) D) Gene expression (Col II, ACAN, SOX9, Col I, and Col X) of BMSCs encapsulated within hydrogel scaffolds by 3D bioprinting after 7 and 14 days' induction. (n= 3, *p< 0.05, **p< 0.01, ***p< 0.001 and ****p< 0.0001) E) Adhesion of BMSCs to the surface of different hydrogels at day 1 and day 4 after F- F-actin and nucleus staining by confocal microscopy.

3.8. Antioxidant capacity of hydrogel scaffolds

H_2O_2 is a common type of ROS that can easily cross the cell membrane and produce highly active free radicals, leading to a series of oxidative stress reactions[39]. Administration of H_2O_2 in cell culture is widely used to study oxidative stress damage to cells. To investigate the antioxidant capacity, BMSCs encapsulated in hydrogel scaffolds were treated with H_2O_2. As shown in Figure 5A, the survival cells in each scaffold were significantly decreased after H_2O_2 treatment. However, a large number of BMSCs were dead for alginate and XG-Fe^{3+} were dead by H_2O_2 treatment. Meanwhile, the protective ability of scaffolds was also evaluated by the live/ dead ratio of BMSCs after H_2O_2 treatment. As shown in Figure 5B, the live/ dead ratio maintained the order of $XGMA_{(H)}$ > collagen > XG-Fe^{3+} > alginate after H_2O_2 stimulation. The difference in the survival ratio before and after H_2O_2 treatment is shown in Figure S9. The difference was observed in the order of alginate > XG-Fe^{3+} > collagen > $XGMA_{(H)}$. The lowest difference ratio corresponded to the best protection ability of the scaffolds against the toxicity of H_2O_2. In particular, a second high difference in survival ratio was observed for XG-Fe^{3+}, and low cell viability existed for XG-Fe^{3+} even without H_2O_2 treatment. We considered that it is the toxicity of Fe^{3+} affects the survival ratio of xanthan gum and reduces its biocompatibility. Therefore, $XGMA_{(H)}$ could effectively protect the cultured BMSCs from the toxicity of H_2O_2, and the presence of Fe^{3+} induced the mortality of BMSCs.

Furthermore, qRT-PCR was used to investigate the expression of antioxidant genes (CAT, SOD, and GSH-Px) in BMSCs to evaluate the antioxidant capacity of different scaffolds. As shown in Figure 5C, the expression of antioxidant genes also increased after H_2O_2 treatment for

all scaffolds. In particular, the expression levels of the corresponding antioxidant genes for $XGMA_{(H)}$ increased to 3.4-fold for CAT, 3.5-fold for SOD, and 3.9-fold for GSH-Px after H_2O_2 treatment, respectively. For all groups, the order of antioxidant gene expression levels was alginate < collagen < XG-Fe^{3+} < $XGMA_{(H)}$. The expression of antioxidant enzymes and MDA was also evaluated by ELISA. As shown in Figure 5D, the expression of antioxidant enzymes (CAT, SOD, and GSH-Px) showed the same trend as the results of qRT-PCR. Notably, the antioxidant enzymes were quite highly expressed for $XGMA_{(H)}$, which increased 11.3-fold for CAT, 2.1-fold for SOD, and 2.0-fold for GSH-Px, after H_2O_2 treatment. The order of antioxidant enzyme expression was alginate < collagen < XG-Fe^{3+} < $XGMA_{(H)}$. However, the H_2O_2-induced MDA expression was lowest for $XGMA_{(H)}$, followed by XG-Fe^{3+}, collagen, and alginate. It is known that the level of MDA, the final breakdown product of membrane lipid peroxidation, can be used as an index to reflect the degree of oxidative damage to cells. Furthermore, ROS fluorescent probes were used for the detection of intracellular ROS. As shown in Figure 5E-H, minimal fluorescence signals were observed in the blank group. However, the fluorescence signals were significantly enhanced under H_2O_2 induction, indicating the generation of a large amount of ROS. Compared with a slight decrease in fluorescence intensity in the alginate group, a significant decrease in fluorescence intensity was observed in the collagen and XG-Fe^{3+} groups, with a better antioxidant effect in the XGMA group. Thus, $XGMA_{(H)}$ had the optimal antioxidant capacity, which was consistent with the results demonstrated in DPPH analysis to scavenge free radicals including $\cdot O_2^-$ and ·OH.[40] It has also been reported that XG exhibited outstanding antioxidant activity and excellent protective effects on H_2O_2-injured Caco-2 cells.[41] Notably, the antioxidant capacity was still preserved for XGMA regardless of MA modification or not. However, the presence of Fe^{3+} in XG-Fe^{3+} induced the death of BMSCs, further leading to poor antioxidant capacity.

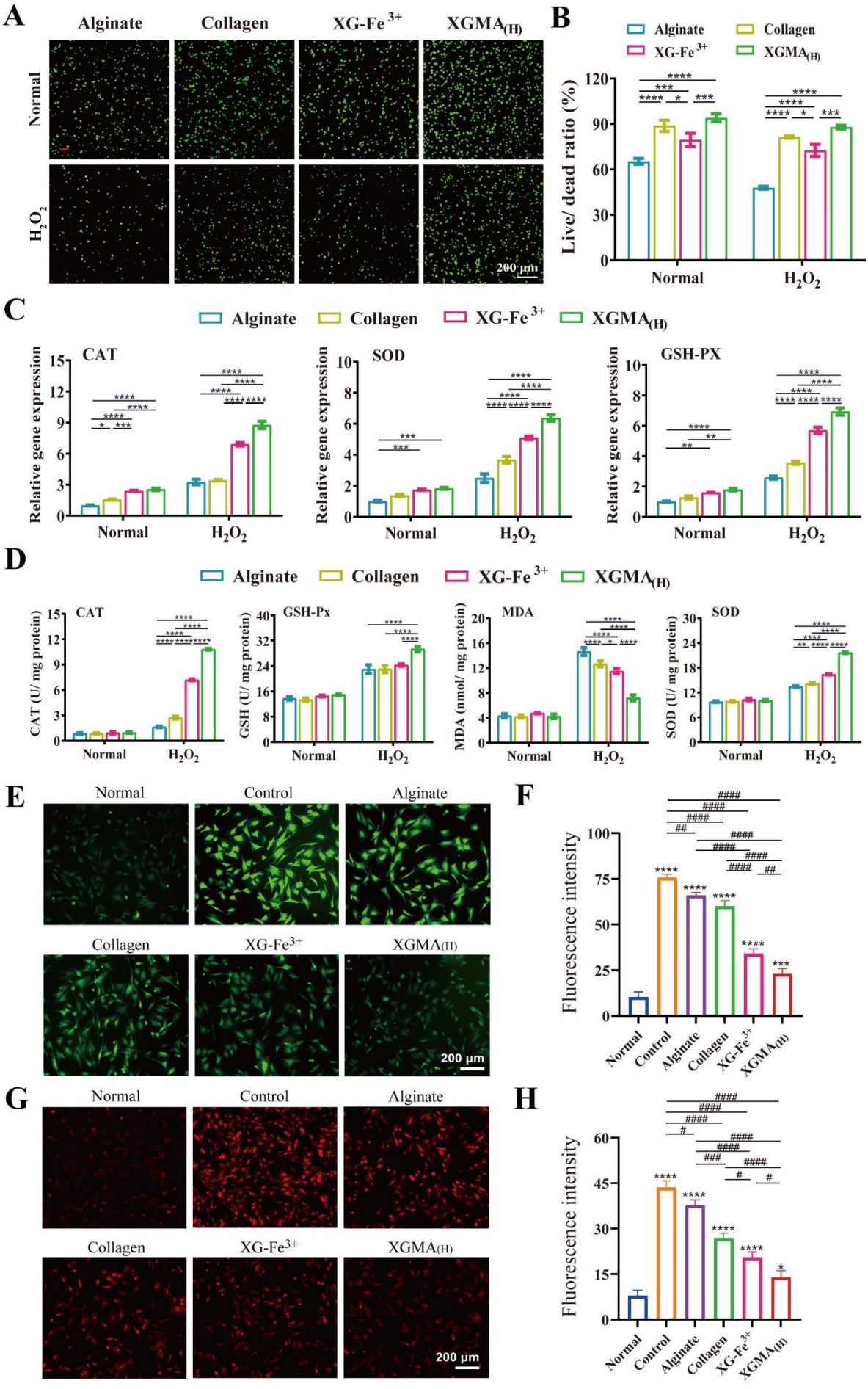
A
Alginate
Collagen
XG-Fe 3+
XGMA(H)
Normal
H2O2
200 μm
B
Alginate
Collagen
XG-Fe 3+
XGMA(H)
Live/ dead ratio (%)
Normal
H2O2
C
Alginate
Collagen
XG-Fe 3+
XGMA(H)
CAT
SOD
GSH-PX
Relative gene expression
Normal
H2O2
D
Alginate
Collagen
XG-Fe 3+
XGMA(H)
CAT (U/ mg protein)
GSH-Px
GSH (U/ mg protein)
MDA
MDA (nmol/ mg protein)
SOD
SOD (U/ mg protein)
Normal
H2O2
E
Normal
Control
Alginate
Collagen
XG-Fe3+
XGMA(H)
200 μm
F
Fluorescence intensity
Normal
Control
Alginate
Collagen
XG-Fe3+
XGMA(H)
G
Normal
Control
Alginate
Collagen
XG-Fe3+
XGMA(H)
200 μm
H
Fluorescence intensity
Normal
Control
Alginate
Collagen
XG-Fe3+
XGMA(H)

Fig. 5. Antioxidant capacity of hydrogel scaffolds. A) Live/ dead staining of H_2O_2-treated BMSCs encapsulated in alginate, collagen, XG-$Fe^{3+,}$ and $XGMA_{(H)}$ and B) the corresponding quantified results. C) Antioxidant gene expression (CAT, SOD, and GSH-Px) of H_2O_2-treated BMSCs encapsulated in alginate, collagen, XG-$Fe^{3+,}$ and $XGMA_{(H)}$ by RT-qPCR. D) Expression of antioxidant enzymes (CAT, SOD, and GSH-Px) and malondialdehyde (MDA) expression in H_2O_2-treated BMSCs encapsulated in alginate, collagen, XG-$Fe^{3+,}$ and $XGMA_{(H)}$ by ELISA. E) Intracellular ROS test using DCFH-DA and F) quantitative analysis. G) Superoxide dismutase assay using NBT and H) quantitative analysis. (n= 3, *#p< 0.05, **##p< 0.01, ***###p< 0.001 and ****####p< 0.0001)

3.9. Post-traumatic cartilage defect repair in vivo

The *in vivo* post-traumatic cartilage defect repair was performed based on a trauma-induced cartilage defect on the rabbit knee joint with a diameter of 4 mm and a depth of 2 mm (Figure S10). The overall evaluation of the knee joint repair was performed after implantation of BMSCs-loaded scaffolds for 3 months. As shown in Figure 6A, almost no inflammation and synovial hyperplasia were observed for all scaffolds compared to the control group, only neochondral tissue was regenerated. Thin fibrous tissue with obvious borders was observed in the control group, indicating the poor self-healing ability of cartilage. For alginate and XG-Fe^{3+}, fibrous cartilage-like tissue was formed within the defect area. On the contrary, for both $XGMA_{(H)}$ and collagen, shiny white repaired tissues with indistinguishable borders were observed, indicating favorable therapeutic effects. According to ICRS macroscopic scoring, the score was 21.0 for $XGMA_{(H)}$, which was significantly higher, being 0.12, 0.15, 0.21, and 2.15 times higher than that of collagen, XG-Fe^{3+}, alginate, and control group, respectively (Figure 6B).

Moreover, the pathological sections were analyzed by hematoxylin & and eosin (HE), Safranin- O/ fast green, and immunohistochemical staining, respectively, for 3 months after surgery. In the control group, it was found that fibrous tissue formed in the defect area with a large residual space interfacing with the original cartilage. In addition, there were some round or oval concave cells characteristic of chondrocytes, and mainly fibrous tissues were observed on the irregular surface for alginate and XG-Fe^{3+}. However, neochondrocytes and a few fibrous tissues were observed for collagen, whereas a large number of newly formed chondrocytes were

observed for $XGMA_{(H)}$ (Figure 6C). Similarly, hyaline cartilage-like tissues with well-integrated surrounding tissues were observed for $XGMA_{(H)}$ compared to other groups by Safranin O/Fast Green staining (Figure 6D). The order of $XGMA_{(H)}$ < collagen < XG-Fe^{3+} < alginate < control was also consistent with the HHGS histologic scoring (Figure 6E). Immunohistochemical staining was also performed to evaluate the Col II expression in each group. As shown in Figure 6F, negative staining was observed in the repaired area of the control group, while a little positive staining appeared for alginate. However, intense positive staining was observed in collagen and $XGMA_{(H)}$, indicating the formation of hyaline cartilage-like tissue.

To investigate the inflammatory response, the inflammatory cells of each group were further observed by light microscopy. As shown in Figure S11A, a few inflammatory cells (with the characteristic of lobulated or irregular distorted nucleus observed) were observed in the control group, while the number of inflammatory cells decreased in the order of alginate < collagen < XG-Fe^{3+} < $XGMA_{(H)}$. After statistical analysis, the ratio of inflammatory cells was 5.8% for the control group, showing a decrease of 27.6%, 41.4%, 58.6%, and 93.1% for alginate, collagen, XG-$Fe^{3+,}$ and $XGMA_{(H)}$, respectively (Figure S11B). In conclusion, $XGMA_{(H)}$ showed the optimal therapeutic effects in trauma-induced cartilage defects with a low risk of PTOA.

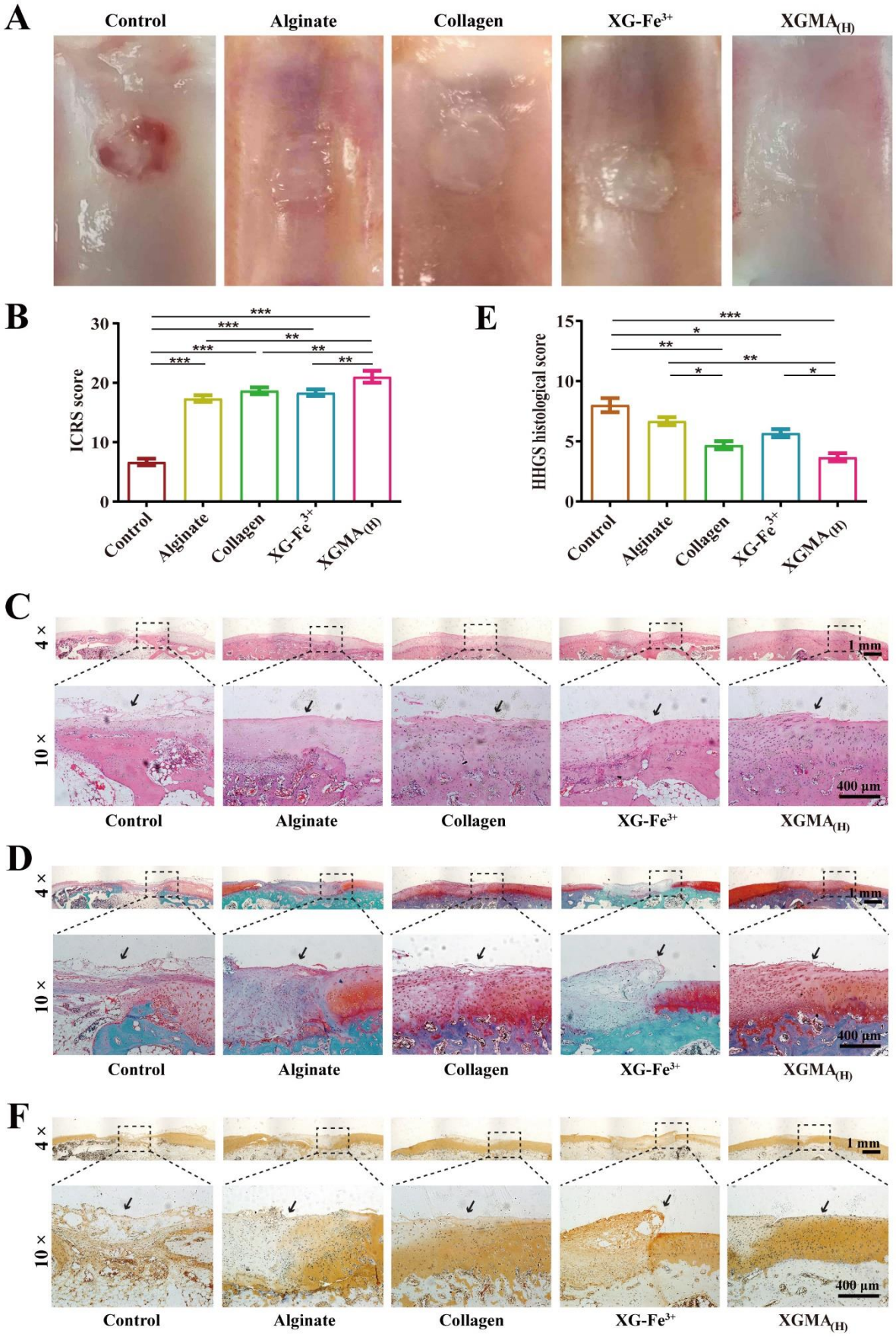

Fig. 6. Therapeutic effects of cartilage defect *in vivo*. A) Macroscopic images of the repair effect of cartilage defect by different hydrogel scaffolds: alginate, collagen, XG-$Fe^{3+,}$ and $XGMA_{(H)}$ and their corresponding International

Cartilage Repair Society (ICRS) macroscopic score. C) Hematoxylin & Eosin (HE) and D) Safranin O/Fast Green staining of knee joint tissue sections at different magnifications and the corresponding histologic/histochemical grading system (HHGS) histologic score (E). F) Immunohistochemical staining of knee joint tissue sections at different magnifications. (n= 6, *p< 0.05, **p< 0.01 and ***p< 0.001)

4. Conclusion

In this work, we synthesized XGMA with interconnected network structure, printability, and shear thinning behavior, which were suitable as bioinks for 3D printing. $XGMA_{(H)}$ with high DS of MA exhibited favorable viscoelastic properties, biocompatibility, and chondrogenic potential, showing great potential for cartilage tissue engineering. Moreover, $XGMA_{(H)}$ possessed remarkable ROS scavenging ability, which could reduce ROS-mediated injury during the cartilage regeneration process and further prevent PTOA. This study provides a novel bioengineering strategy for cartilage tissue engineering by using 3D bioprinted antioxidant scaffolds.

Supporting Information

Figure S1 Rheological behaviors of different pre-gel solutions; Figure S2 SEM images of XGMA(H); Figure S3 Macroscopic images of various hydrogel scaffolds; Figure S4 Macroscopic images of multilayer XGMA(H); Figure S5 Macroscopic images of 3D printed XGMA(H); Figure S6 Stress-strain curve of XGMA(H); Figure S7 ROS scavenging capacity of hydrogel scaffolds; Figure S8 3D reconstructed live/dead images; Figure S9 Survival of inflammatory BMSCs; Figure S10 Images of a hydrogel scaffold implanted in a joint defect; Figure S11 The result of the inflammatory cell count.

Declarations

Ethics approval and consent to participate

Thirty New Zealand Large White rabbits were used in this study, with no gender requirements, and all animal experiments met animal ethics requirements and were approved by the Ethics Committee of Guangxi Medical University. (No: 201606190).

Data availability

The authors declare that all data supporting the results of this study are available in the article and its supplementary information files, or from the corresponding author upon reasonable request.

Conflict of interest

The authors declare that they have no conflict of interest.

Acknowledgments

We are very grateful to the Animal Experiment Center of Guangxi Medical University for raising the rats used in this study. This work was supported by the Guangxi Science and Technology Base and Talent Special Project (Grant No. GuikeAD21075002), Natural Science Foundation of Guangxi (Grant No. 2020GXNSFAA159134), National Natural Science Foundation of China (Grant No. 82160430), Guangxi Science and Technology Major Project (Grant No. GuikeAA19254002), and Nanning Qingxiu District Science and Technology Major Special Project (Grant No. 2020013). This research is supported by the RIE2025 MTC Individual Research Grants (M22K2c0085), administered by the Agency of Science, Technology and Research (A*STAR).

Author contributions

Yuting Chen, Yiguan Le, and Junxu Yang: Project administration, Conceptualization, Visualization, Methodology, Writing - Original Draft. Yifeng Yang and Xianjing Feng: Formal analysis, Investigation, Methodology. Jinhong Cai and Yifeng Shang: Resources, Investigation, Methodology. Sugiarto: Investigation, Writing - Review & Editing. Qingjun Wei, Dan Kai, Li Zheng, and Jinmin Zhao: Supervision, Conceptualization, Writing - Review & Editing.

References

(1) S.K. Bedingfield, J.M. Colazo, M. Di Francesco, F. Yu, D.D. Liu, V. Di Francesco, L.E. Himmel, M.K. Gupta, H. Cho, K.A. Hasty, P. Decuzzi, C.L. Duvall. Top-Down Fabricated microPlates for Prolonged, Intra-articular Matrix Metalloproteinase 13 siRNA Nanocarrier Delivery to Reduce Post-traumatic Osteoarthritis. *ACS Nano* **2021**, *15*, 14475-14491.
(2) C. Deng, Q. Zhou, M. Zhang, T. Li, H. Chen, C. Xu, Q. Feng, X. Wang, F. Yin, Y. Cheng, C. Wu. Bioceramic Scaffolds with Antioxidative Functions for ROS Scavenging and Osteochondral Regeneration. *Advanced Science* **2022**, *9*.
(3) M.B. Gugjoo, M.-U.R. Fazili, M.A. Gayas, R.A. Ahmad, K. Dhama. Animal mesenchymal stem cell research in cartilage regenerative medicine – a review. *Veterinary Quarterly* **2019**, *39*, 95-120.
(4) K. Zha, X. Li, Z. Yang, G. Tian, Z. Sun, X. Sui, Y. Dai, S. Liu, Q. Guo. Heterogeneity of mesenchymal stem cells in cartilage regeneration: from characterization to application. *npj Regenerative Medicine* **2021**, *6*.
(5) S. Jiang, G. Tian, Z. Yang, X. Gao, F. Wang, J. Li, Z. Tian, B. Huang, F. Wei, X. Sang, L. Shao, J. Zhou, Z. Wang, S. Liu, X. Sui, Q. Guo, W. Guo, X. Li. Enhancement of acellular cartilage matrix scaffold by Wharton's jelly mesenchymal stem cell-derived exosomes to promote osteochondral regeneration. *Bioactive Materials* **2021**, *6*, 2711-2728.
(6) S. Critchley, E.J. Sheehy, G. Cunniffe, P. Diaz-Payno, S.F. Carroll, O. Jeon, E. Alsberg, P.A.J. Brama, D.J. Kelly. 3D printing of fibre-reinforced cartilaginous templates for the regeneration of osteochondral defects. *Acta Biomaterialia* **2020**, *113*, 130-143.
(7) J.J. Kochumalayil, M. Bergenstråhle-Wohlert, S. Utsel, L. Wågberg, Q. Zhou, L.A. Berglund. Bioinspired and Highly Oriented Clay Nanocomposites with a Xyloglucan Biopolymer Matrix: Extending the Range of Mechanical and Barrier Properties. *Biomacromolecules* **2012**, *14*, 84-91.
(8) J. Huang, Y. Jiang, Y. Liu, Y. Ren, Z. Xu, Z. Li, Y. Zhao, X. Wu, J. Ren. Marine-inspired molecular mimicry generates a drug-free, but immunogenic hydrogel adhesive protecting surgical anastomosis. *Bioactive Materials* **2021**, *6*, 770-782.
(9) Q. Chen, X. Mei, G. Han, P. Ling, B. Guo, Y. Guo, H. Shao, G. Wang, Z. Cui, Y. Bai, F. Xu. Xanthan gum protects rabbit articular chondrocytes against sodium nitroprusside-induced apoptosis in vitro. *Carbohydrate Polymers* **2015**, *131*, 363-369.
(10) C.-S. Wang, N. Virgilio, P.J. Carreau, M.-C. Heuzey. Understanding the Effect of Conformational Rigidity on Rheological Behavior and Formation of Polysaccharide-Based Hybrid Hydrogels. *Biomacromolecules* **2021**, *22*, 4016-4026.
(11) A. Masek, E. Chrzescijanska, M. Latos, M. Zaborski. Influence of hydroxyl substitution on flavanone antioxidants properties. *Food Chemistry* **2017**, *215*, 501-507.
(12) H. Shao, G. Han, P. Ling, X. Zhu, F. Wang, L. Zhao, F. Liu, X. Liu, G. Wang, Y. Ying, T. Zhang. Intra-articular injection of xanthan gum reduces pain and cartilage damage in a rat osteoarthritis model. *Carbohydrate Polymers* **2013**, *92*, 1850-1857.
(13) L. Mei, B. Shen, J. Xue, S. Liu, A. Ma, F. Liu, H. Shao, J. Chen, Q. Chen, F. Liu, Y. Ying, P. Ling. Adipose tissue–derived stem cells in combination with xanthan gum attenuate osteoarthritis progression in an experimental rat model. *Biochemical and Biophysical Research Communications* **2017**, *494*, 285-291.
(14) G. Han, Q. Chen, F. Liu, Z. Cui, H. Shao, F. Liu, A. Ma, J. Liao, B. Guo, Y. Guo, F. Wang, P. Ling, X. Mei. Low molecular weight xanthan gum for treating osteoarthritis. *Carbohydrate Polymers* **2017**, *164*, 386-395.
(15) R. Zhang, Y. Tao, Q. Xu, N. Liu, P. Chen, Y. Zhou, Z. Bai. Rheological and ion-conductive properties of injectable and self-healing hydrogels based on xanthan gum and silk fibroin. *International Journal of Biological Macromolecules* **2020**, *144*, 473-482.

(16) A. Kumar, K.M. Rao, S.S. Han. Application of xanthan gum as polysaccharide in tissue engineering: A review. *Carbohydrate Polymers* **2018**, *180*, 128-144.
(17) X. Han, Q. Liang, A. Rashid, A. Qayum, A. Rehman, M. Zhong, Y. Sun, Y. Liu, H. Ma, S. Miao, X. Ren. The effects of different hydrocolloids on lotus root starch gelatinization and gels properties. *International Journal of Biological Macromolecules* **2024**, *257*.
(18) H. Pan, B. Zheng, H. Shen, M. Qi, Y. Shang, C. Wu, R. Zhu, L. Cheng, Q. Wang. Strength-tunable printing of xanthan gum hydrogel via enzymatic polymerization and amide bioconjugation. *Chemical Communications* **2020**, *56*, 3457-3460.
(19) M. Kang, O. Oderinde, S. Liu, Q. Huang, W. Ma, F. Yao, G. Fu. Characterization of Xanthan gum-based hydrogel with Fe3+ ions coordination and its reversible sol-gel conversion. *Carbohydrate Polymers* **2019**, *203*, 139-147.
(20) B.A. Nerger, P.T. Brun, C.M. Nelson. Microextrusion printing cell-laden networks of type I collagen with patterned fiber alignment and geometry. *Soft Matter* **2019**, *15*, 5728-5738.
(21) G. Montalbano, S. Fiorilli, A. Caneschi, C. Vitale-Brovarone. Type I Collagen and Strontium-Containing Mesoporous Glass Particles as Hybrid Material for 3D Printing of Bone-Like Materials. *Materials* **2018**, *11*.
(22) M.P.J. van den Borne, N.J.H. Raijmakers, J. Vanlauwe, J. Victor, S.N. de Jong, J. Bellemans, D.B.F. Saris. International Cartilage Repair Society (ICRS) and Oswestry macroscopic cartilage evaluation scores validated for use in Autologous Chondrocyte Implantation (ACI) and microfracture. *Osteoarthritis and Cartilage* **2007**, *15*, 1397-1402.
(23) P. Mainil-Varlet, B. Van Damme, D. Nesic, G. Knutsen, R. Kandel, S. Roberts. A New Histology Scoring System for the Assessment of the Quality of Human Cartilage Repair: ICRS II. *The American Journal of Sports Medicine* **2010**, *38*, 880-890.
(24) L. Ouyang, R. Yao, Y. Zhao, W. Sun. Effect of bioink properties on printability and cell viability for 3D bioplotting of embryonic stem cells. *Biofabrication* **2016**, *8*.
(25) H. Li, Y.J. Tan, S. Liu, L. Li. Three-Dimensional Bioprinting of Oppositely Charged Hydrogels with Super Strong Interface Bonding. *ACS Applied Materials & Interfaces* **2018**, *10*, 11164-11174.
(26) A.M. Duraj-Thatte, A. Manjula-Basavanna, J. Rutledge, J. Xia, S. Hassan, A. Sourlis, A.G. Rubio, A. Lesha, M. Zenkl, A. Kan, D.A. Weitz, Y.S. Zhang, N.S. Joshi. Programmable microbial ink for 3D printing of living materials produced from genetically engineered protein nanofibers. *Nature Communications* **2021**, *12*.
(27) L. Zhang, G. Yang, B.N. Johnson, X. Jia. Three-dimensional (3D) printed scaffold and material selection for bone repair. *Acta Biomaterialia* **2019**, *84*, 16-33.
(28) J. Wei, B. Wang, Z. Li, Z. Wu, M. Zhang, N. Sheng, Q. Liang, H. Wang, S. Chen. A 3D-printable TEMPO-oxidized bacterial cellulose/alginate hydrogel with enhanced stability via nanoclay incorporation. *Carbohydrate Polymers* **2020**, *238*.
(29) S. Paek, C. Roldán‐Carmona, K.T. Cho, M. Franckevičius, H. Kim, H. Kanda, N. Drigo, K.H. Lin, M. Pei, R. Gegevičius, H.J. Yun, H. Yang, P.A. Schouwink, C. Corminboeuf, A.M. Asiri, M.K. Nazeeruddin. Molecular Design and Operational Stability: Toward Stable 3D/2D Perovskite Interlayers. *Advanced Science* **2020**, *7*.
(30) G. Janarthanan, H.S. Shin, I.-G. Kim, P. Ji, E.-J. Chung, C. Lee, I. Noh. Self-crosslinking hyaluronic acid–carboxymethylcellulose hydrogel enhances multilayered 3D-printed construct shape integrity and mechanical stability for soft tissue engineering. *Biofabrication* **2020**, *12*.
(31) N. Huebsch, P.R. Arany, A.S. Mao, D. Shvartsman, O.A. Ali, S.A. Bencherif, J. Rivera-Feliciano, D.J. Mooney. Harnessing traction-mediated manipulation of the cell/matrix interface to control stem-cell fate. *Nature Materials* **2010**, *9*, 518-526.
(32) M. Yue, Y. Liu, P. Zhang, Z. Li, Y. Zhou. Integrative Analysis Reveals the Diverse Effects of 3D Stiffness upon Stem Cell Fate. *International Journal of Molecular Sciences* **2023**, *24*.

(33) A. Lee1, A.R.H. , D.J.S. , J.W.T. , T.J.H. , S.Y. , , J.M. Bliley1, P.G.C. , 2, A. W. Feinberg1,3. 3D bioprinting of collagen to rebuild components of the human heart.pdf. *Science* **2019**, 482-487.
(34) J. Leppiniemi, P. Lahtinen, A. Paajanen, R. Mahlberg, S. Metsä-Kortelainen, T. Pinomaa, H. Pajari, I. Vikholm-Lundin, P. Pursula, V.P. Hytönen. 3D-Printable Bioactivated Nanocellulose–Alginate Hydrogels. *ACS Applied Materials & Interfaces* **2017**, *9*, 21959-21970.
(35) X. Yang, Z. Lu, H. Wu, W. Li, L. Zheng, J. Zhao. Collagen-alginate as bioink for three-dimensional (3D) cell printing based cartilage tissue engineering. *Materials Science and Engineering: C* **2018**, *83*, 195-201.
(36) W. Dai, N. Kawazoe, X. Lin, J. Dong, G. Chen. The influence of structural design of PLGA/collagen hybrid scaffolds in cartilage tissue engineering. *Biomaterials* **2010**, *31*, 2141-2152.
(37) D. Hua, S. Gao, M. Zhang, W. Ma, C. Huang. A novel xanthan gum-based conductive hydrogel with excellent mechanical, biocompatible, and self-healing performances. *Carbohydrate Polymers* **2020**, *247*.
(38) L. Sun, M. Li, T. Gong, J. Feng. Preparation and evaluation of an innovative antibacterial bi-layered composite dressing for skin wound healing. *Journal of Tissue Viability* **2021**, *30*, 454-461.
(39) D.B. Goodenowe, J. Haroon, M.A. Kling, M. Zielinski, K. Mahdavi, B. Habelhah, L. Shtilkind, S. Jordan. Targeted Plasmalogen Supplementation: Effects on Blood Plasmalogens, Oxidative Stress Biomarkers, Cognition, and Mobility in Cognitively Impaired Persons. *Frontiers in Cell and Developmental Biology* **2022**, *10*.
(40) X. Xiong, M. Li, J. Xie, Q. Jin, B. Xue, T. Sun. Antioxidant activity of xanthan oligosaccharides prepared by different degradation methods. *Carbohydrate Polymers* **2013**, *92*, 1166-1171.
(41) A. Faralli, E. Shekarforoush, F. Ajalloueian, A.C. Mendes, I.S. Chronakis. In vitro permeability enhancement of curcumin across Caco-2 cells monolayers using electrospun xanthan-chitosan nanofibers. *Carbohydrate Polymers* **2019**, *206*, 38-47.